Low NF and High P1dB Wideband Quasi-Circulator With Unequal Power Split and Reconfigurable Inter-Stage Matching

Wen Chen, *Graduate Student Member, IEEE*, Zhixian Deng, *Graduate Student Member, IEEE*, Yiyang Shu, *Graduate Student Member, IEEE*, Huizhen Jenny Qian, *Member, IEEE*, and Xun Luo, *Senior Member, IEEE*

***Abstract*— In this article, a wideband quasi-circulator (QC) with the low noise figure (NF) and high 1-dB compression point (P_{1dB}) is proposed. The slotline-based 180° hybrid is introduced to achieve the wideband high transmitter-receiver (TX-RX) isolation. Meanwhile, the bidirectional in-phase stage and the nonreciprocal out-of-phase stage are utilized to obtain specific power-split ratios for the low insertion loss and high antenna-transmitter (ANT-TX) isolation. By using the unequal power split, the proposed QC is without the fundamental 3-dB loss seen in reciprocal ANT interfaces. Besides, to further enhance the TX-RX isolation within a wideband, a reconfigurable inter-stage matching network based on a varactor-tuned capacitor is implemented. To verify the mechanisms mentioned above, a reconfigurable wideband QC operating at 1.75–2.9 GHz is implemented and fabricated. The total power consumption is 224 mW. The measurement exhibits in-band TX-RX isolation of 27–58 dB. The TX-ANT and ANT-RX insertion losses are 4.3–5.0 dB and 1.0–1.9 dB, respectively. The QC also achieves the minimum in-band ANT-RX NF of 3.4 dB. Meanwhile, the measured TX-ANT and ANT-RX IIP3s are 39.4 and 32.5 dBm, respectively. The TX input P_{1dB} is greater than 28.78 dBm, while the RX input P_{1dB} is 23 dBm. The TX-induced ANT-RX P_{1dB} is measured to be 28 dBm.**

***Index Terms*— 180° hybrid full-duplex (FD), quasi-circulator (QC), reconfigurable circuits, wideband.**

I. Introduction

With the ever-increasing demand for high data rates in modern wireless communications, there are urgent requirements of wireless channels with large capacity and high spectral efficiency in recent years. To satisfy the practical requirements, either time or frequency division duplexing systems are employed [1], [2]. However, all these systems are exclusively half-duplex, which limits the maximum transmission rate to only half of the network capacity. For this reason, the full-duplex (FD) system is introduced to double the spectral efficiency of wireless systems. The FD radio is widely known as a simultaneously transmit and receive capable radio since it enables the transmitter (TX) and receiver (RX) to operate at the same time and over the same frequency. Such operation substantially alleviates the radio spectrum allocation burden, thereby yielding uncompromised communication data capacity [3]–[7]. One of the entire challenges of an FD transceiver is that transmitted signals can directly feed into the RX chain, which will cause self-interference and severely diminish the RX's dynamic range. To avoid such self-interference, a pair of antennas (ANTs) in the RF/analog domain is introduced with the drawback of large size [8]. Then, the FD transceiver with a shared ANT is investigated. Such operation seems to be more feasible in the FD system for the minimized ANT size and can be easily used in multiple-input, multiple-output applications. The electrical balance duplexers (EBDs) are utilized to achieve the high TX-RX isolation [9]–[11]. However, such duplexers feature a fundamental minimum 3-dB loss due to their reciprocity.

Recently, circulators and quasi-circulators (QCs) have been widely developed as a transceiver front-end with a shared ANT interface. The conventional ferromagnetic circulator [12] is presented with good isolation and return loss, however, in the sacrifice of high cost and bulky size. To minimize the size of the circuit, active QCs are developed [13]–[15], which are with the drawback of relatively high noise figure (NF) and limited power handling. To improve the NF and power handling performances, passive circulators are proposed [16]–[20]. Nevertheless, the requirement of the additional modulated LO signals increases the system complexity. Recently, QCs using the combined active and passive circuits are developed with advantages of design flexibility and good performance [21]–[25]. As shown in Fig. 1(a), a tunable QC using the compact fully reconfigurable 180° hybrid and amplifier stages is proposed to improve the isolation performance [25]. However, such a combined-type of QC suffers from the fundamental 3-dB path loss introduced by the reciprocal passive devices, while the operation frequency range still needs to be further expanded. Therefore, the circulator or QC design with the merits of the wide bandwidth, low NF, and high power handling still remains a great challenge.

Manuscript received September 30, 2020; revised December 31, 2020; accepted January 3, 2021. Date of publication February 22, 2021; date of current version April 2, 2021. This work was supported in part by the National Natural Science Foundation of China under Grant 61934001 and Grant 61904025. *(Corresponding author: Xun Luo.)*

The authors are with the Center for Advanced Semiconductor and Integrated Micro-System, University of Electronic Science and Technology of China, Chengdu 611731, China (e-mail: xun-luo@ieee.org).

Color versions of one or more figures in this article are available at https://doi.org/10.1109/TMTT.2021.3058602.

Digital Object Identifier 10.1109/TMTT.2021.3058602

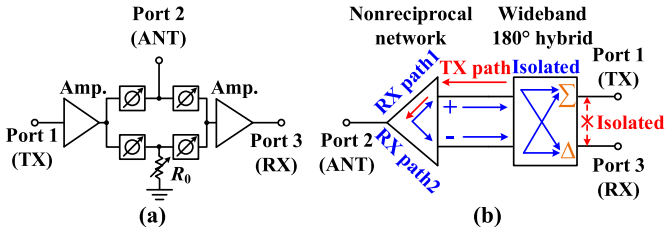

Fig. 1. (a) Configuration of the conventional combined-type QC [25]. (b) Topology of the proposed wideband QC.

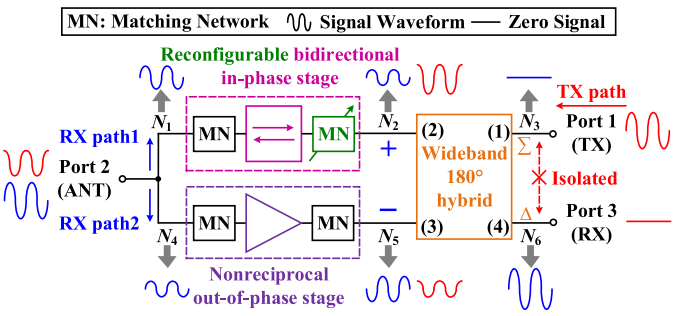

Fig. 2. Principle and configuration of the proposed QC.

As depicted in Fig. 1(b), a wideband QC with the low RX NF and high 1-dB compression point ($P_{1\,dB}$) is proposed in our conference article [26]. Such QC utilizes a nonreciprocal network connecting to a 180° hybrid to achieve the ANT-TX reverse isolation instead of using an amplifier. Thus, the amplifier's limitation of TX power handing could be avoided. In this work, the wideband 180° hybrid is presented to achieve the wide operation band and high TX-RX isolation. Meanwhile, a bidirectional in-phase stage based on the common-gate (CG) stage and a nonreciprocal out-of-phase stage based on the common-source (CS) stage are introduced, which obtain specific power-split ratios for the low insertion loss and high ANT-TX isolation. To the authors' best knowledge, it is the first time that the QC uses the unequal power split without additional modulated signals to omit the fundamental 3-dB loss seen in reciprocal ANT interfaces, while achieves low NF and high $P_{1\,dB}$.

Compared to the previous work in [26], a deep analysis using the power transmission method is proposed and the simplified model of the architecture is extracted in this article. Based on the theoretical analysis, a reconfigurable inter-stage matching network and a step-impedance 180° hybrid are utilized to further improve the TX-RX isolation and the operation bandwidth, respectively. This article is organized as follows. In Section II, the architecture and operation principle of the proposed QC using unequal power split is presented. A prototype QC is implemented by a wideband 180° hybrid, a CG-stage, and a CS-stage in Section III. The proposed reconfigurable wideband QC is measured and compared with state of the art in Section IV. The conclusion is summarized in Section V.

II. Architecture and Principle

A. System Architecture

Fig. 2 shows the principle and configuration of the proposed reconfigurable wideband QC. It is composed of a wideband 180° hybrid, a reconfigurable bidirectional in-phase stage, and a nonreciprocal out-of-phase stage. Port (1) is the sum port and Port (4) is the difference port of such hybrid, which connect to the TX and RX Ports, respectively. Besides, the bidirectional in-phase stage and nonreciprocal out-of-phase stage are connected to the hybrid by the inter-stage matching networks, respectively. Note that from left to right, the gain of the out-of-phase stage is larger than that of the in-phase stage and the signals are out-of-phase at the right outputs. Differently, from right to left, the signal is blocked at the out-of-phase stage due to the nonreciprocity and could only transmit through the in-phase stage.

The proposed QC utilizes the unequal power split to reduce the trade-off between the TX insertion loss and RX NF. Here, the unequal power-split situations appear at the 180° hybrid and the T-junction of the ANT Port, respectively. For transmit mode operation, ideally, the TX input signal is split into two paths with unequal magnitude by the 180° hybrid. Then, by optimizing the load impedance of Port (3), a larger than half portion of the TX signal is transmitted to Port (2), and the remaining portion is transmitted to Port (3), respectively. Thus, the lower TX insertion loss could be achieved. Since the signal transmits from Port (1) is suppressed at Port (4) of the 180° hybrid, the TX signal is canceled at the RX Port. For receive mode operation, the signal from ANT Port is divided into two paths, which are defined as RX path1 and RX path2, respectively. Then, larger than half of the RX signal is transmitted to the RX path1 and the rest is transmitted to the RX path2. Here, the signals in RX path are depicted at each critical node shown in Fig. 2 (i.e., N_1, N_2, N_3, N_4, N_5, and N_6). In RX path1, due to the non-inverting for the signal of the in-phase stage, the signals are in-phase at the N_1 and N_2. Besides, in RX path2, the signal is inverted at the output of the out-of-phase stage. Thus, at the N_2 and N_5, the signals are out-of-phase. By implementing the out-of-phase stage with specific transmission gain, the differential-mode signal could be canceled at Port (1), which represents the high ANT-TX isolation. Meanwhile, it is worth pointing out that the more power transmit to the RX path1, the larger gain of the out-of-phase stage is required to obtain the high ANT-TX isolation, which leads to lower RX NF. Therefore, due to the unequal power split with the out-of-phase stage's power compensation, both lower TX insertion loss and RX NF of the QC could be achieved. Incidentally, the RX-ANT isolation is relatively low due to the in-phase stage reciprocity. However, this is not so important considering that the input signal is usually not from RX Port [27].

Therefore, based on the aforementioned principles, the QC function is achieved by combining the wideband 180° hybrid, bidirectional in-phase stage, and nonreciprocal out-of-phase stage. The TX-RX isolation is provided by the 180° hybrid, and the ANT-TX isolation is introduced by the bidirectional in-phase stage with nonreciprocal out-of-phase stage, respectively. Besides, the unequal power split is utilized to reduce the trade-off between the TX insertion loss and RX

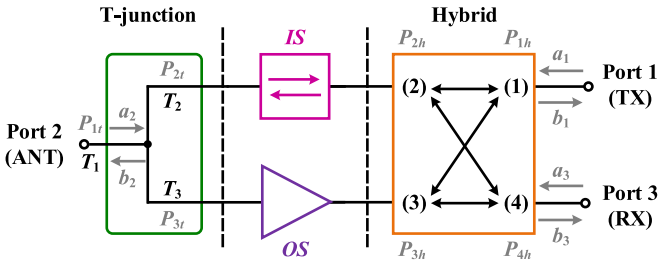

Fig. 3. Block diagram of the proposed QC.

NF. To investigate the mechanism of the proposed reconfigurable wideband QC, the three-layer dielectric substrate (i.e., $\varepsilon_{r1,3} = 3.66$ and $\varepsilon_{r2} = 3.55$ with thickness of $h_{1,3} = 0.508$ mm and $h_2 = 0.1$ mm), full-wave EM-simulator IE3D, and ADS are used.

B. Operation

The block diagram of the proposed QC and the power at critical nodes are shown in Fig. 3, where the matching networks are omitted. The P_{ih} is power at terminal (i) of the hybrid ($i = 1, 2, 3, 4$). Besides, the P_{1t} is power at the ANT Port (i.e., T_1). The P_{2t} and P_{3t} are power at inputs of the in-phase stage and out-of-phase stage (i.e., T_2 and T_3), respectively. Meanwhile, the a_i are incident waves and the b_i are reflected waves. For simplicity, assuming the QC is lossless and all terminations are matched, while the wideband 180° hybrid has high isolation.

Input signal a_1 at the TX Port is split into upper and lower branches. Then, a portion of the upper signal is transmitted to the ANT Port by the in-phase stage and a T-junction. The transmitter power at the ANT Port could be derived as

$$P_{b_2,\mathrm{TX}} = (|H_{21h,\mathrm{TX}}||H_{\mathrm{IS}}||H_{12t,\mathrm{TX}}|)P_{a_1,\mathrm{TX}} \tag{1}$$

where $H_{21h,\mathrm{TX}}$ is the power transmission coefficient from Port (1) to Port (2) of the hybrid in TX path, H_{IS} is the power transmission coefficient of the in-phase stage, and $H_{12t,\mathrm{TX}}$ is the power transmission coefficient from T_2 to T_1 of the T-junction in TX path. Note that the TX-ANT transmission parameter (i.e., $P_{b_2,\mathrm{TX}}$ / $P_{a_1,\mathrm{TX}}$) is related to the $H_{21h,\mathrm{TX}}$ of the hybrid and $H_{12t,\mathrm{TX}}$ of the T-junction. The $|H_{21h,\mathrm{TX}}|$ and $|H_{12t,\mathrm{TX}}|$ could be expressed as

$$|H_{21h,\mathrm{TX}}| = \frac{P_{2h,\mathrm{TX}}}{P_{1h,\mathrm{TX}}} \tag{2}$$

$$|H_{12t,\mathrm{TX}}| = \frac{P_{1t,\mathrm{TX}}}{P_{2t,\mathrm{TX}}}. \tag{3}$$

For a signal a_2 entering the ANT Port, assuming the interconnected mismatch is ignored, the power received by the TX Port can be derived by

$$P_{b_1,\mathrm{RX}} = (|H_{21t,\mathrm{RX}}||H_{\mathrm{IS}}||H_{12h,\mathrm{RX}}| - |H_{31t,\mathrm{RX}}||H_{\mathrm{OS}}||H_{13h,\mathrm{RX}}|)P_{a_2,\mathrm{RX}}. \tag{4}$$

Here, $H_{21t,\mathrm{RX}}$ is the power transmission coefficient from T_1 to T_2 of the T-junction in RX path, H_{OS} is the power transmission coefficient of the out-of-phase stage, and $H_{12h,\mathrm{RX}}$ is the power transmission coefficient from Port (2) to Port (1) of the hybrid in RX path. The $|H_{21t,\mathrm{RX}}|$ and $|H_{12h,\mathrm{RX}}|$ could be expressed as

$$|H_{21t,\mathrm{RX}}| = \frac{P_{2t,\mathrm{RX}}}{P_{1t,\mathrm{RX}}} \tag{5}$$

$$|H_{12h,\mathrm{RX}}| = \frac{P_{1h,\mathrm{RX}}}{P_{2h,\mathrm{RX}}}. \tag{6}$$

Similarly, the $|H_{31t,\mathrm{RX}}|$ and $|H_{13h,\mathrm{RX}}|$ could be obtained. To achieve the high ANT-TX isolation, ideally, the $P_{b_1,\mathrm{RX}}$ in (4) should be 0, which leads to the following condition:

$$|H_{21t,\mathrm{RX}}||H_{\mathrm{IS}}||H_{12h,\mathrm{RX}}| = |H_{31t,\mathrm{RX}}||H_{\mathrm{OS}}||H_{13h,\mathrm{RX}}|. \tag{7}$$

Due to the reciprocity of the hybrid, the relation between the power transmission coefficients in the TX path and RX path of the hybrid could be as

$$|H_{i1h,\mathrm{TX}}| = |H_{1ih,\mathrm{RX}}| \tag{8}$$

where $i = 2$ or 3. Then, (7) can be rewritten as

$$|H_{\mathrm{OS}}| = \frac{P_{2h,\mathrm{TX}}}{P_{3h,\mathrm{TX}}} \times \frac{P_{2t,\mathrm{RX}}}{P_{3t,\mathrm{RX}}} \times |H_{\mathrm{IS}}|. \tag{9}$$

Since the ANT-TX is isolated, the received signals are recombined constructively at the RX Port. Thus, the power received by the RX Port can be derived as

$$P_{b_3,\mathrm{RX}} = (|H_{21t,\mathrm{RX}}||H_{\mathrm{IS}}| + |H_{31t,\mathrm{RX}}||H_{\mathrm{OS}}|)P_{a_2,\mathrm{RX}}. \tag{10}$$

Therefore, to achieve the lower RX insertion loss, the power-split ratio of the T-junction represented by k_1 should satisfy the following condition:

$$k_1 = \frac{P_{2t,\mathrm{RX}}}{P_{3t,\mathrm{RX}}} > 1. \tag{11}$$

Meanwhile, according to (1) and (2), to obtain the lower TX insertion loss, the power-split ratio of the hybrid represented by k_2 should meet the following requirement:

$$k_2 = \frac{P_{2h,\mathrm{TX}}}{P_{3h,\mathrm{TX}}} > 1. \tag{12}$$

Then, the relationship between the transmission parameters of the QC (i.e., $|S_{21}|$ and $|S_{32}|$) and the power-split ratios (i.e., k_1 and k_2) can be simply expressed as

$$|S_{21}| = 10\log_{10}\left(\frac{k_1}{1+k_1}\frac{k_2}{1+k_2}\right) \tag{13}$$

$$|S_{32}| = 10\log_{10}\frac{k_1(1+k_2)}{(1+k_1)}. \tag{14}$$

Note that for equal power split (i.e., $k_1 = 1$ and $k_2 = 1$), the calculated $|S_{21}|$ is -6 dB and the $|S_{32}|$ is 0 dB, which indicates the inherent 3-dB path loss provided by the reciprocal approaches. Fig. 4 shows the calculated $|S_{21}|$ and $|S_{32}|$ versus power-split ratios k_1 and k_2 according to (13) and (14). Here, (9) is satisfied and $|H_{\mathrm{IS}}| = 1$. It can be seen that by properly choosing the k_1 and k_2, the TX insertion loss could be lower than 3 dB and the RX gain is larger than 0 dB simultaneously. However, it doesn't exhibit zero TX-ANT loss fundamentally because the signal from TX to ANT through the out-of-phase path is completely blocked.

The proposed structure may also exhibit a system insertion gain due to the large $|H_{\mathrm{OS}}|$. The overall circuit stability

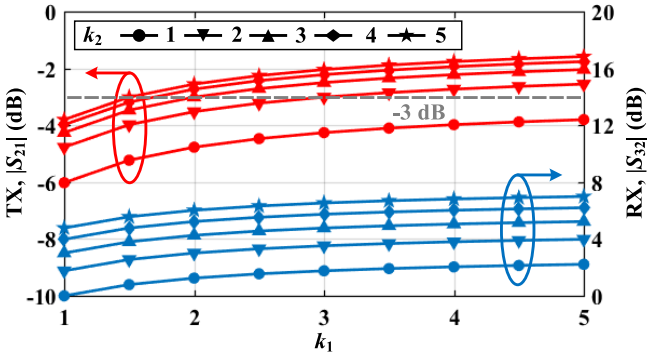

Fig. 4. Calculated TX-ANT and ANT-RX transmission parameters ($|S_{21}|$ and $|S_{32}|$) versus power-split ratios k_1 and k_2 ($S_{12} = 0$ and $|H_{IS}| = 1$).

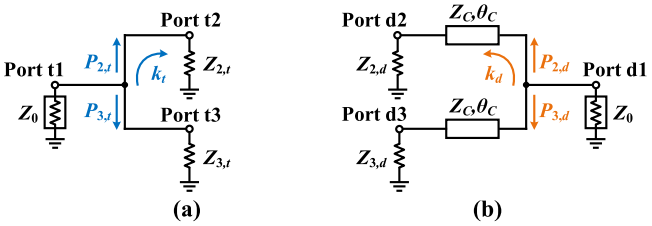

Fig. 5. Circuits used for required power-split ratio. (a) General T-junction. (b) Divider with $\lambda/4$ transmission lines.

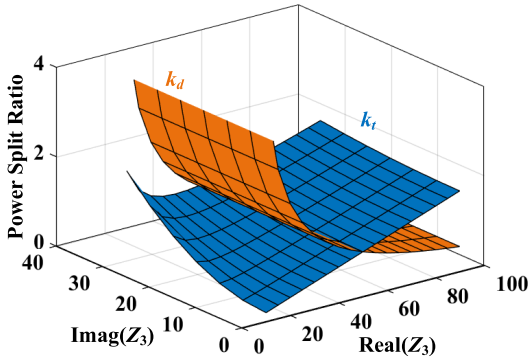

Fig. 6. Calculated power-split ratios k_t and k_d with the corresponding various Z_3 ($Z_0 = 50\ \Omega$, $Z_2 = 50\ \Omega$, $Z_C = 70.7\ \Omega$, and $\theta_C = 90°$).

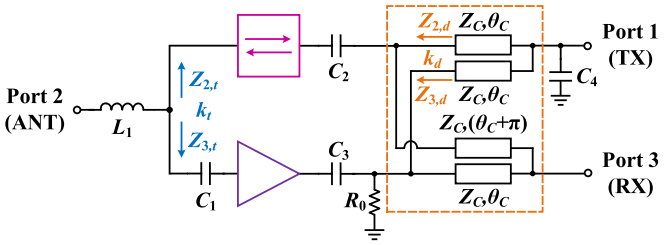

Fig. 7. Simplified model of the QC with ideal transmission line.

directly depends on the gain of the out-of-phase stage and the isolation of the 180° hybrid (i.e., $|S_{23,h}|$). The internal loop may exhibit an open-loop gain higher than unity, which leads to the potential onset of oscillations. The loop gain of the positive feedback system could be simply expressed as $|S_{32,n}||S_{23,h}|$, where the $|S_{32,n}|$ is the gain from in-phase stage to out-of-phase stage. If the loop gain is smaller than 1, the overall system gain is finite, leading to the following condition:

$$|S_{32,n}||S_{23,h}| < 1. \tag{15}$$

Due to $|S_{32,n}|$ is positively correlated with $|H_{OS}|$, the value of the $|H_{OS}|$ cannot be too large.

As shown in Fig. 5, two circuits (i.e., a general T-junction and a divider with $\lambda/4$ transmission lines) with different load impedance relationships are utilized to obtain the required power-split ratio. The relations between the power-split ratio and the load impedance of the two circuits are expressed as follows:

$$k_t = \frac{P_{2,t}}{P_{3,t}} = \left| \frac{\text{Real}(Z_{2,t})}{\text{Real}(Z_{3,t})} \times \frac{Z_{3,t}^2}{Z_{2,t}^2} \right| \tag{16}$$

$$k_d = \frac{P_{2,d}}{P_{3,d}} = \left| \frac{\text{Real}\left(Z_C^2/Z_{2,d}\right)}{\text{Real}\left(Z_C^2/Z_{3,d}\right)} \times \frac{\left(Z_C^2/Z_{3,d}\right)^2}{\left(Z_C^2/Z_{2,d}\right)^2} \right| \tag{17}$$

where $Z_{i,t}$ is the load impedance of the T-junction and $Z_{i,d}$ is the load impedance of the divider ($i = 2, 3$). The detailed derivation is given by (19)–(24) in the Appendix. It can be seen that the k_t is unaffected by the ANT voltage standing wave ratio (VSWR). Note that as shown in Fig. 6, the k_t and k_d show the opposite trend while the load impedance changes.

The simplified model of the proposed QC is depicted in Fig. 7 to further analyze the operating principle. Such a model consists of ideal transmission lines, no-noise amplifier models, and impedance matching circuits. To obtain the larger k_t and k_d simultaneously, the design procedures are summarized as follows: Firstly, the $Z_{3,t}$ is designed for the larger k_t to achieve lower RX insertion loss. Secondly, the $Z_{3,d}$ is implemented for the larger k_d to achieve lower TX insertion loss. Finally, the gain of the out-of-phase amplifier (i.e., $|H_{21,OA}|$) is chosen to compensate the unequal power-split ratios k_t and k_d for high ANT-TX isolation. Thus, the trade-off between the TX and RX insertion losses could be reduced. The C_1, C_3, and R_0 are designed for desired power-split ratios k_t and k_d. Besides, the capacitor C_2 is introduced to tune the phase-imbalance in the RX path and the impedance $Z_{2,d}$ for higher isolation. Meanwhile, the L_1 and C_4 are utilized for ports matching, respectively.

Fig. 8(a) shows the simulated TX-ANT transmission parameter ($|S_{21}|$) and RX NF of the QC using the proposed simplified model. Here, the in-phase amplifier is assumed to be lossless (i.e., $H_{12,IA} = H_{21,IA} = 1$). Note that the TX insertion loss and RX NF could simultaneously be lower than 3 dB at 2.3 GHz, which indicates the proposed QC is without fundamental 3-dB loss seen in reciprocal ANT interfaces. Meanwhile, as shown in Fig. 8(b), the return loss of all ports is better than −10 dB. Fig. 9 shows the effects of the gain $|H_{21,OA}|$ on the load impedance $Z_{3,d}$, the ANT-RX stability factor (K_{23}), and S-parameters with RX NF, respectively. As shown in Fig. 9(a), the real part of $Z_{3,d}$ decreases sharply as the $|H_{21,OA}|$ increases, which leads to the larger k_d from (17). Besides, the larger $|H_{21,OA}|$ could obtain lower RX NF.

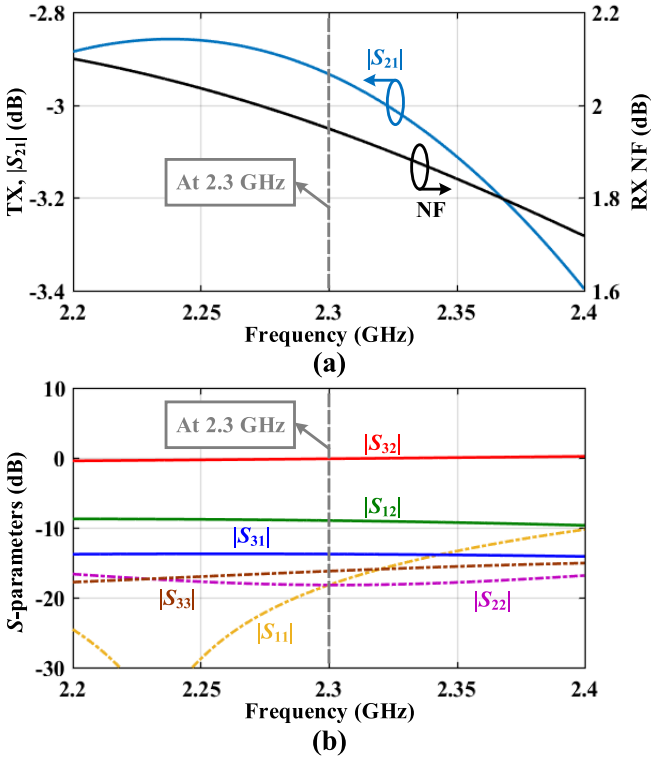

Fig. 8. Simulated results of the QC using the proposed simplified model. (a) TX-ANT transmission parameter ($|S_{21}|$) and RX NF. (b) S-parameters ($L_1 = 2$ nH, $C_1 = 0.4$ pF, $C_2 = 1.6$ pF, $C_3 = 0.4$ pF, $C_4 = 1.4$ pF, $R_0 = 70\ \Omega$, $H_{12,\mathrm{IA}} = H_{21,\mathrm{IA}} = 1$, $H_{21,OA} = 5e^{j100}$, $Z_C = 70.7\ \Omega$, and $\theta_C = 90°$ at 2.3 GHz).

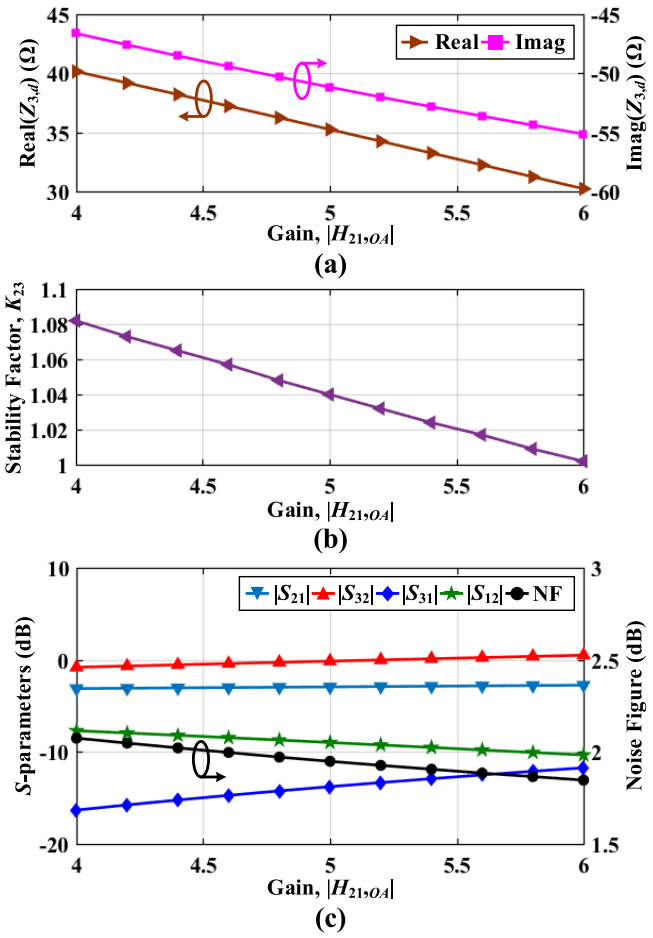

Fig. 9. Simulated (a) $Z_{3,d}$, (b) ANT-RX stability factor (K_{23}), and (c) S-parameters and NF versus gain $|H_{21,\mathrm{OA}}|$ at 2.3 GHz.

Thus, lower TX-ANT insertion loss and RX NF could be achieved simultaneously. However, as depicted in Fig. 9(b), the ANT-RX stability factor (K_{23}) becomes worse with the increasing of $|H_{21,\mathrm{OA}}|$. Meanwhile, due to the unequal power split of the proposed hybrid, there will be an impedance mismatch in the TX path while looking into the out-of-phase amplifier output. The TX leakage signal reflected back by the out-of-phase amplifier could degrade the TX-RX isolation. As shown in Fig. 9(c), the increase of the $|H_{21,\mathrm{OA}}|$ leads to the TX-RX isolation reduction. Therefore, there is a trade-off between the low insertion loss and high TX-RX isolation.

III. Circuit Implementation

Based on the principle investigated in Section II, a reconfigurable wideband QC based on a wideband 180° hybrid, a reconfigurable bidirectional in-phase stage, and a nonreciprocal out-of-phase stage is implemented in a three-layer dielectric substrate (i.e., $\varepsilon_{r1,3} = 3.66$ and $\varepsilon_{r2} = 3.55$ with thickness of $h_{1,3} = 0.508$ mm and $h_2 = 0.1$ mm). The design procedures of the proposed QC are summarized as follows: Firstly, a wideband 180° hybrid is implemented for the wide operation band and high TX-RX isolation. Secondly, a bidirectional in-phase stage based on the CG-stage and a nonreciprocal out-of-phase stage based on the CS-stage are utilized to obtain the high ANT-TX isolation. Finally, a reconfigurable inter-stage matching network based on the varactor-tuned capacitor is introduced to further enhance the TX-RX isolation under different operating frequencies.

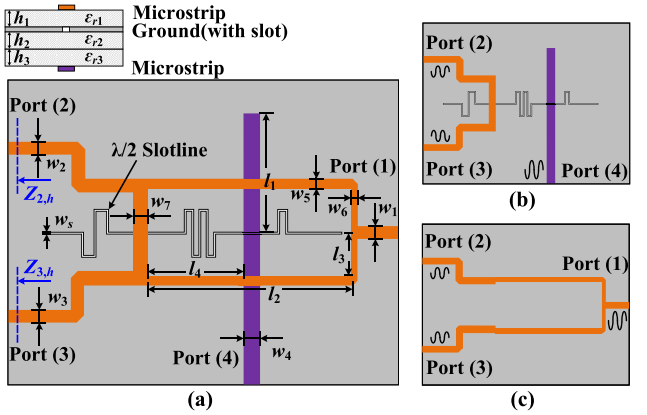

Fig. 10. (a) Layout of the wideband 180° hybrid. ($w_1 = w_2 = w_3 = w_7 = 1.14$, $w_4 = 1.3$, $w_5 = 0.78$, $w_6 = 0.58$, $w_s = 0.2$, $l_1 = 12.4$, $l_2 = 19.4$, $l_3 = 4.4$, and $l_4 = 8.86$, unit: mm). (b) Out-of-phase case. (c) In-phase case.

A. Wideband 180° Hybrid

The layout of the wideband 180° hybrid is shown in Fig. 10(a), which is formed on a three-layer substrate. Note that a slot is etched in the middle metal-ground. The Ports

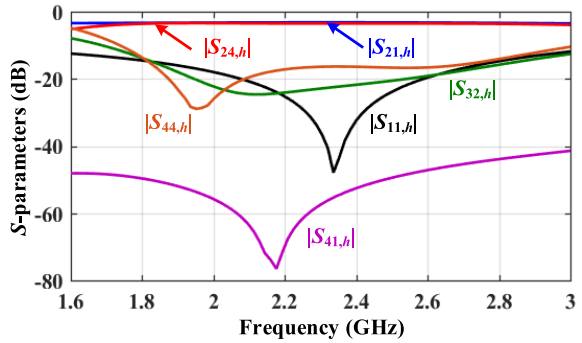

Fig. 11. Simulated S-parameters of the wideband 180° hybrid.

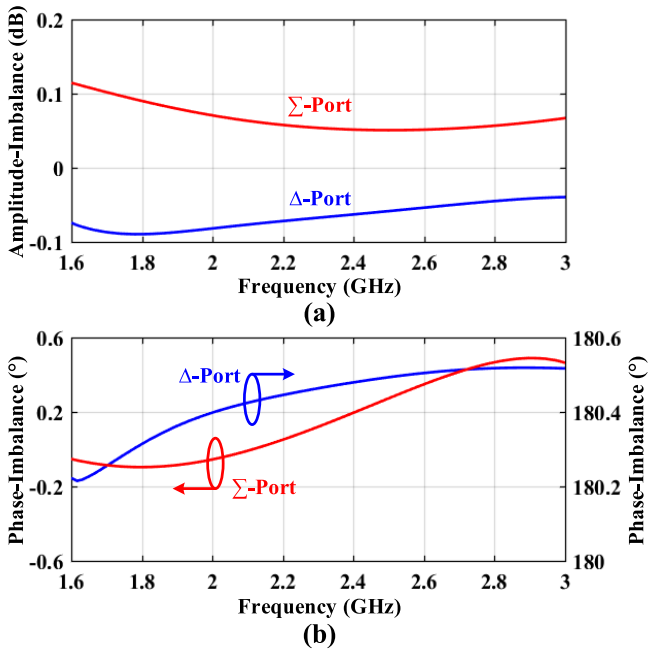

Fig. 12. Simulated imbalance characteristics of the wideband 180° hybrid. (a) Amplitude-imbalance. (b) Phase-imbalance.

(1)–(3) are on the top layer, while Port (4) is on the bottom layer, respectively.

Such a hybrid can be regarded as an assembly of out-of-phase and in-phase dividers/combiners. For the out-of-phase case in Fig. 10(b), the signal from Port (4) is coupled to Ports (2) and (3) through the slot. Due to the inherent property of the slot [12], the divided signals at Ports (2) and (3) are out-of-phase. For the in-phase case in Fig. 10(c), the signal from Port (1) is split into two lines at the T-junction. Then, due to the symmetry of the two lines, the divided signals at Port (2) and Port (3) are in-phase. Once the hybrid is operated as a combiner, the in-phase signal from Ports (2) and (3) is canceled at Port (4), and similarly, the out-of-phase signal is disappeared at Port (1). The width of the slot is optimized based on the analysis in [28] and the slot is designed as a meander-shape for size miniaturization. The parameters w_4, l_1, and l_4 are optimized for improving the return loss of Port (4). Besides, the parameters w_1, w_5, w_6, l_2, and l_3 are optimized carefully to improve the power dividing performance. Here, the step-impedance design method (i.e., w_5 is not equal to w_6) is introduced to further wider the operation bandwidth.

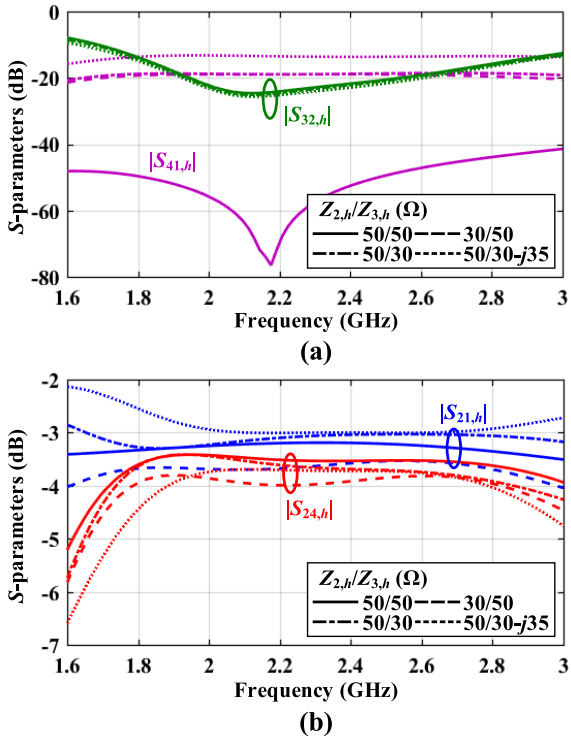

Fig. 13. Simulated S-parameters of the wideband 180° hybrid with different loaded impedances at Port (2) $Z_{2,h}$ and Port (3) $Z_{3,h}$. (a) Isolation parameters ($|S_{41,h}|$ and $|S_{32,h}|$). (b) Transmission parameters ($|S_{21,h}|$ and $|S_{24,h}|$).

The simulated S-parameters of the proposed 180° hybrid are depicted in Fig. 11. It is notable that high isolation within the wide frequency range of 1.6–3 GHz is achieved. Fig. 12 shows the amplitude- and phase-imbalances responses of Ports (2) and (3), while the hybrid is operated as a divider. The amplitude-imbalances of the in-phase case and out-of-phase case are both less than 0.2 dB and the phase-imbalances are both less than 0.6°, which indicates a good in-band balance performance.

As shown in Fig. 13, the varied load impedance $Z_{2,h}$ and $Z_{3,h}$ at Port (2) and Port (3) show negligible influence on the isolation $|S_{32,h}|$ of the hybrid. Meanwhile, the insertion losses $|S_{21,h}|$, $|S_{24,h}|$, and isolation $|S_{41,h}|$ of the hybrid are affected by the load impedances of Port (2) and Port (3). Note that the path losses of the hybrid and the inter-stage impedance matching will affect the TX power efficiency and the RX NF of the QC [12], which should be taken into consideration in the design of the proposed QC with the optimized performance.

B. CG-Stage and CS-Stage

The CG-stage and CS-stage are employed to realize the bidirectional in-phase stage and nonreciprocal out-of-phase stage, respectively. The CG-stage is utilized to produce 0° phase shift for signal and wideband matching for ANT Port [29]. Besides, the CS-stage is introduced to produce a 180° phase shift for signal and nonreciprocal amplify. Meanwhile, the CG-CS noise-canceling technique is used to cancel the thermal noise of the CG-transistor in the RX path [30], which further reduces the RX NF. Fig. 14 shows the configuration of the CG-stage and CS-stage. The GaAs high electron mobility transistors are

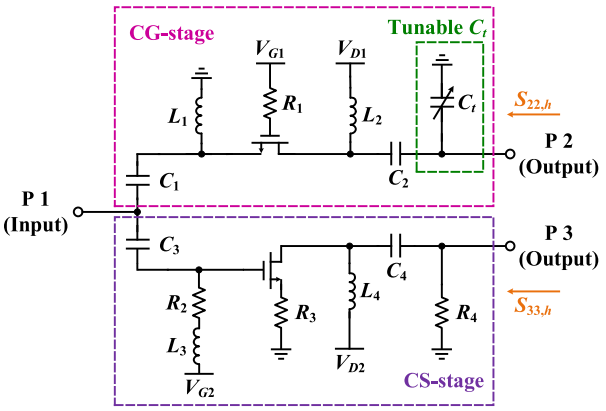

Fig. 14. Configuration of the CG-stage and CS-stage.

widely used in microwave amplifier design due to their good characteristics. Thus, the GaAs FET ATF-34143 from Avago, high Q capacitors, and RF inductors from Murata are utilized to implement the CG-stage and CS-stage.

The bias voltage V_{G1} and V_{D1} are configured for low conduction loss of the CG-stage. The optimized bias V_{G2} and V_{D2} are chosen to achieve the required gain of the CS-stage. Besides, the input impedance of the CG-stage is implemented for wideband ANT Port matching, while the input impedance of the CS-stage is designed for required power-split ratio k_1 and low RX NF. The capacitor C_3 could be used to trade the TX insertion loss and RX insertion loss. Meanwhile, the output impedances of the CG-stage and CS-stage are matched to the proposed wideband 180° hybrid, which obtains the required power-split ratio k_2 and low interconnected loss. By properly designing the CG-stage and CS-stage, a good phase-balance performance at the CG-CS stage outputs could be achieved. Thus, the received signals are recombined constructively at the RX Port, while the thermal noise of the CG-transistor could be canceled. Moreover, the source negative feedback resistor R_3 of the CS-stage is introduced to enhance the stability. Since the gain of CS-stage can be controlled by the gate voltage V_{G2} of the CS amplifier, the potential instability can be taken care of by reducing the V_{G2} of the CS amplifier. Due to the principles of the proposed hybrid are similar to a rat-race coupler, the balance condition to achieve high isolation could be expressed as

$$\Gamma_{2,h} = \Gamma_{3,h}. \tag{18}$$

Therefore, a tunable C_t is utilized to obtain higher TX-RX isolation versus operating frequency by tuning the input impedance of the P 2.

Fig. 15 shows the simulated phase-imbalance of the outputs P 2 and P 3 versus the C_t. The phase-imbalance is less than 8° and the best balance performance could be tuned by the C_t. Besides, as depicted in Fig. 16, the input impedance of the P 2 varies with the tuning capacitor C_t. Note that at a relatively low frequency range, the larger C_t leads to the lower difference between $S_{22,h}$ and $S_{33,h}$. However, this trend is opposite at the higher frequency range. Thus, to achieve the high TX-RX isolation versus different operating frequency, the larger C_t should be chosen at a relatively low-frequency range, while the lower C_t should be chosen at a relatively high-frequency

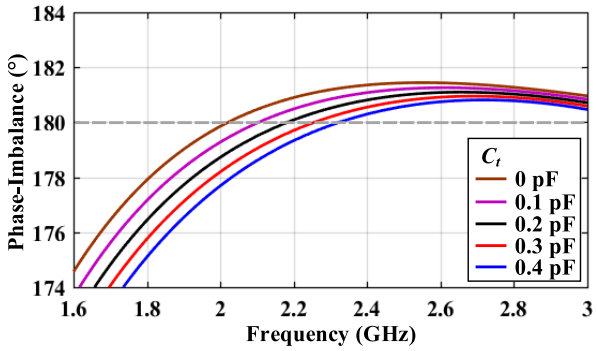

Fig. 15. Simulated phase-imbalance of the outputs versus the C_t, where the I/O port are terminated to 50 Ω (L_1 = 2.4 nH, L_2 = L_3 = L_4 = 20 nH, C_1 = 33 pF, C_2 = 2.2 pF, C_3 = 0.6 pF, C_4 = 0.8 pF, R_1 = R_2 = 4.7 kΩ, R_3 = 24 Ω, R_4 = 91 Ω, V_{G1} = V_{G2} = 1 V, V_{D1} = 0.1 V, and V_{D2} = 4 V).

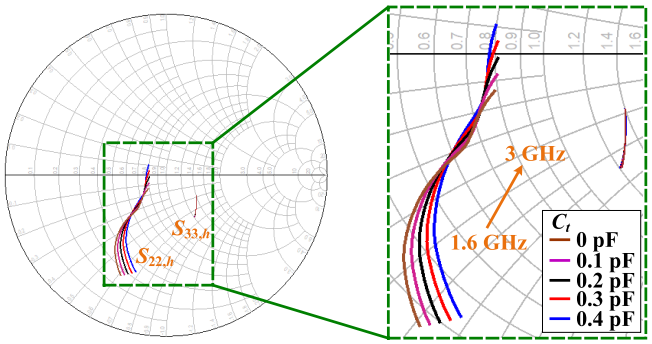

Fig. 16. Simulated input impedance of the P 2 and P 3 under cases of various C_t.

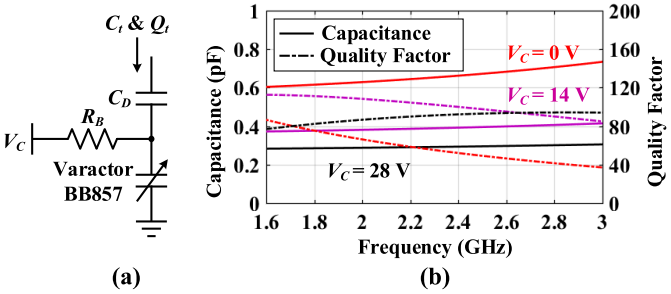

Fig. 17. (a) Configuration of the C_t. (b) Simulated capacitance and quality factor of the C_t versus control voltage (C_D = 0.6 pF and R_B = 10 kΩ).

range. Fig. 17(a) depicts the configuration of the C_t used in the inter-stage matching network, which is a dc-block capacitor C_D in series with a varactor (i.e., BB857 from Infineon). The control voltage V_C is fed by a 10-kΩ resistor R_B. It is worth pointing out that there is a trade-off between the tuning range and quality factor of the C_t [25]. Then, an optimized C_D = 0.6 pF (i.e., GRM1555 series capacitors from Murata, with Q_D = 124 at 2.35 GHz) is chosen for the tunable C_t implementation. The simulated characteristics of the C_t are shown in Fig. 17(b).

C. Reconfigurable Wideband QC

The configuration of the proposed QC is depicted in Fig. 18. Here, the 10- and 0.3-pF capacitors are added for TX and RX Ports matching due to the effects of parasitism, respectively. Fig. 19 shows the simulated TX-RX isolation versus control voltage. To achieve the maximum isolation at the different operating frequency, the V_C is chosen as 0 V

TABLE I
PERFORMANCE SUMMARY AND COMPARISON WITH STATE-OF-THE-ARTS

Ref.	TMTT 2016 [10]	MWCL 2017 [15]	JSSC 2018 [11]	IMS 2019 [18]	TCAS-I 2019 [25]	RFIC 2020 [19]	JSSC 2020 [20]	**This Work**
Architecture	EBD	QC	EBD [1]	Circulator	QC	Circulator	Circulator	**QC**
Technology	180-nm SOI CMOS	45-nm CMOS SOI	180-nm SOI CMOS	0.2-um GaN	PCB	65-nm CMOS	180-nm SOI CMOS	**PCB**
Frequency (GHz)	1.9 to 2.2	5.3 to 7.3	0.7 to 1	0.1 to 1	2.9 to 3.56	DC to 1	0.914 to 1.086	**1.75 to 2.9**
BW (%)	14.6	31.7	35.3	163	21.1	200	17.2	**49.5**
TX-RX Isolation (dB)	>40	30 to 42	>40 [2]	>18 [3]	34 to 49	>18	>25	**27 to 58**
TX-ANT, $\|S_{21}\|$ (dB)	-3.7 to -3.4	<10.5	-3.9 to -3.7	-4.1 to -3	6.8 to 7.1	-4.3 to -3.1	-2.07 [4,6]/ -2.1 [5,6]	**-5.0 to -4.3**
ANT-RX, $\|S_{32}\|$ (dB)	-3.9 to -3.8	<-5	1.1 to 1.8	-4.1 to -3	4.3 to 4.9	-4.3 to -3.1	-2.49 [4,6]/ -2.6 [5,6]	**-1.9 to -1.0**
RX NF (dB)	3.9	20	8.7 to 9.2	N/R	4.8 to 5.5	3.1 to 4.1	2.5	**3.4 to 4.5**
Support Z_{ANT} (VSWR)	1.5:1	N/R	2.3:1	N/R	N/R	N/R	2.33:1	**1.3:1** [7]
TX-ANT IP_{1dB} (dBm)	>27	4.5	32.5	17	21.7 [8]	1.4	34	**>28.78** [9]
ANT-RX IP_{1dB} (dBm)	>27	N/R	N/A	17	N/R	1.4	17.3	**23**
TX-ANT IIP3 (dBm)	70	20	70	N/R	17.7	20	50.3	**39.4**
ANT-RX IIP3 (dBm)	72	N/R	6.4	N/R	N/R	20	36.5	**32.5**
TX-induced ANT-RX P_{1dB} (dBm)	N/R	N/R	N/A	N/R	N/R	6.2	29.3 [4]/ 28.4 [5]	**28**
Amplifiers Requirement	N/A	TX	RX	N/A	TX&RX	N/A	N/A	**N/A**
LO Signals	N/A	N/A	N/A	Require	N/A	Require	Require	**N/A**
Power Consumption (mW)	0	415	62.5	4100	830	20	104 [4]/ 39 [5]	**224**
Size	λ_g^2/1092 1.74 mm^2	λ_g^2/121 1.57 mm^2	λ_g^2/504 14.4 mm^2	λ_g^2/1798 18.5 mm^2	λ_g^2/4.3 1130 mm^2	λ_g^2/159664 0.19 mm^2	λ_g^2/805 9 mm^2	**λ_g^2/2.3 1974 mm^2**

[1]EBD with switched LC LNA. [2]Isolation BW is 0.4%. [3]Calculated from measurement plot. [4]Supply voltage is 2 V. [5]Supply voltage is 1.5 V. [6]Transmission loss at the center frequency. [7]Estimated from measurement plot (>20 dB TX-RX isolation). [8]Output P_{1dB}. [9]Limited by the test setup.

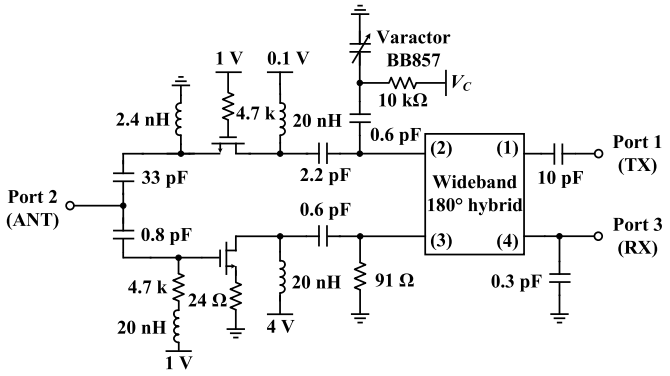

Fig. 18. Configuration of the proposed QC.

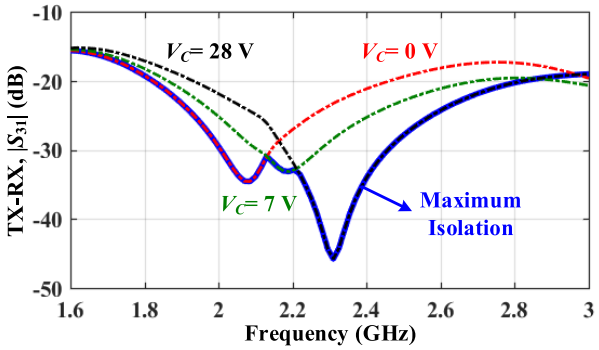

Fig. 19. Simulated TX-RX isolation versus control voltage.

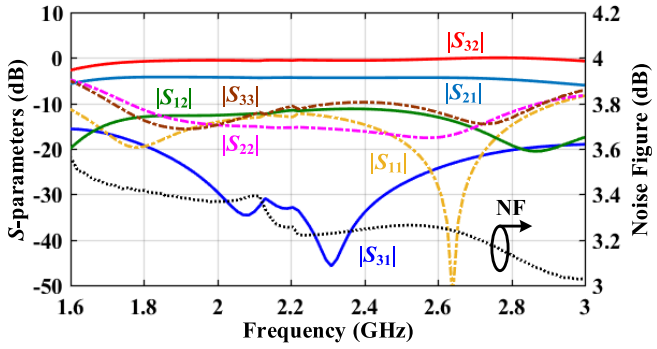

Fig. 20. Simulated S-parameters and RX NF of the QC with optimized control voltage (V_C = 0 V in 1.6–2.13 GHz, V_C = 7 V in 2.13–2.2 GHz, and V_C = 28 V in 2.2–3 GHz).

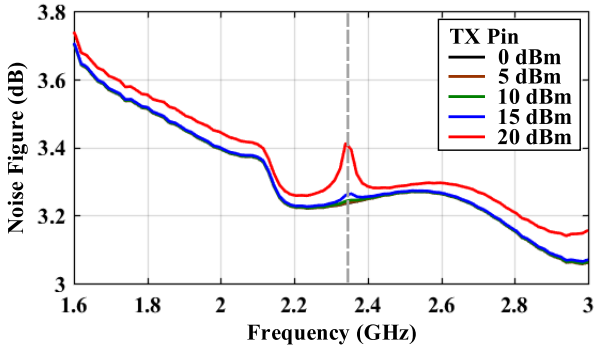

Fig. 21. Simulated RX NF under different TX input power, where the TX signal frequency is 2.35 GHz (V_C = 28 V).

in 1.6–2.13 GHz, 7 V in 2.13–2.2 GHz, and 28 V in 2.2–3 GHz. The −20-dB TX-RX isolation fractional bandwidth of the proposed QC is larger than 40%. Besides, as shown in Fig. 20, the RX NF is lower than 3.6 dB within the frequency range of 1.6–3 GHz. To further investigate the performance of the proposed QC in the FD wireless application, the NF of the RX-path is evaluated while the transmitter is operating. Fig. 21 shows that the in-band RX NF degenerates slightly with the increasing of TX power. The probable reason is the signal-noise ratio degeneration due to the TX leakage.

IV. FABRICATION AND MEASUREMENT

Based on the mechanisms and circuits mentioned above, a reconfigurable wideband QC is fabricated and measured.

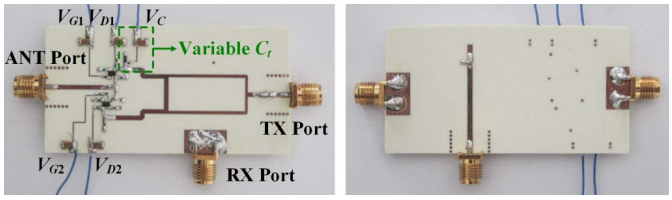

Fig. 22. Photographs of the fabricated QC. (a) Top view. (b) Bottom view.

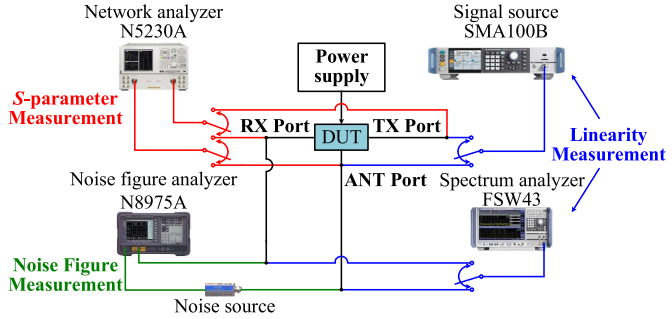

Fig. 23. Measurement setup.

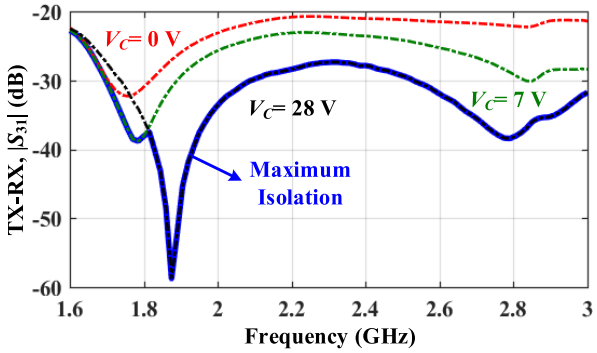

Fig. 24. Measured TX-RX isolation versus control voltage.

The photograph of the proposed QC is illustrated in Fig. 22 and the total circuit size is 61.7 mm × 32 mm (i.e., 0.925 λ_g × 0.479 λ_g, where λ_g is the microstrip guided wavelength at 2.35 GHz). Fig. 23 shows the measurement setup. The *S*-parameters are measured by the N5230A network analyzer. Besides, the NF is performed using the N4002A noise source and N8975A NF analyzer. Meanwhile, the large-signal performances are measured by the Rohde & Schwarz SMA100B signal generator and FSW43 spectrum analyzer.

As depicted in Fig. 24, the maximum TX-RX isolation varies with the control voltage V_C. To obtain the higher TX-RX isolation, the V_C is chosen as 7 V at a lower frequency range, while the V_C is chosen as 28 V at a higher frequency range. Fig. 25 shows the measured *S*-parameters of the proposed QC with optimized control voltage V_C. The measured TX-RX isolation is 27–58 dB over the operating frequency range of 1.75–2.9 GHz. Besides, the in-band TX insertion loss is 4.3–5.0 dB and the RX insertion loss is 1.0–1.9 dB. Here, the difference between simulation and measurement is mainly caused by the component tolerances and the solders used in fabrication. Meanwhile, the TX reversed isolation is greater than 10 dB and the return loss of the TX, ANT, and RX Ports are all better than −10 dB, respectively. The total power

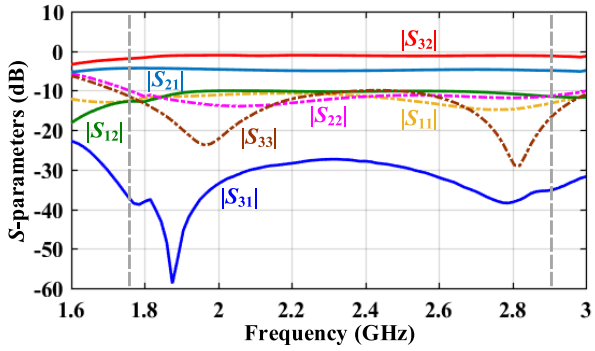

Fig. 25. Measured *S*-parameters of the proposed QC with optimized control voltage (V_C = 7 V in 1.6–1.82 GHz and V_C = 28 V in 1.82–3 GHz).

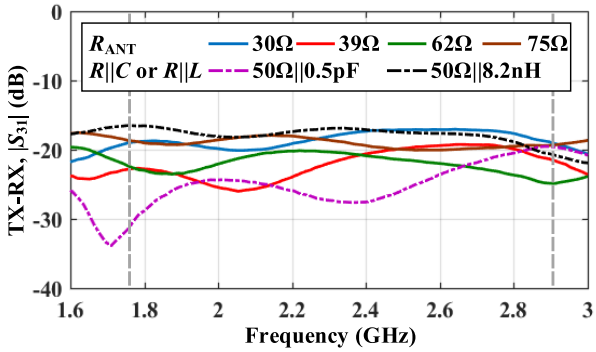

Fig. 26. Measured TX-RX isolation under various loaded impedances at ANT Port.

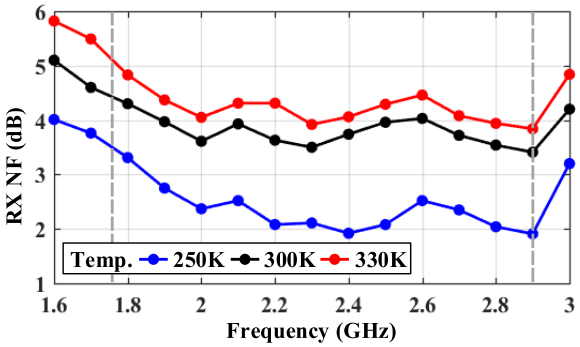

Fig. 27. Measured RX NF of the proposed QC with optimized control voltage under different temperatures of 250, 300, and 330 K.

consumption is 224 mW (i.e., 220 mW at CS-stage and 4 mW at CG-stage). Fig. 26 shows the measured TX-RX isolation under various loaded impedances at ANT Port. The ANT VSWR of 1.3:1 is estimated from the measurement plot to support 20-dB TX-RX isolation. Note that since the impedance tuner is unavailable, the loaded impedance at ANT Port is varied by the different combinations of resistors, inductors, and capacitors. The TX-RX isolation under different ANT VSWR can be improved by introducing an ANT impedance balancer or tuner [20], [25]. The SCAL 70CTR3 is used for RX NF measurement under different temperatures. As depicted in Fig. 27, the measured in-band RX NFs are 1.9–3.5 dB, 3.4–4.5 dB, and 3.8–5.1 dB under different temperatures of 250, 300, and 330 K with optimized control voltage V_C, respectively. To further improve the losses and NF performances, a bidirectional nonreciprocal out-of-phase

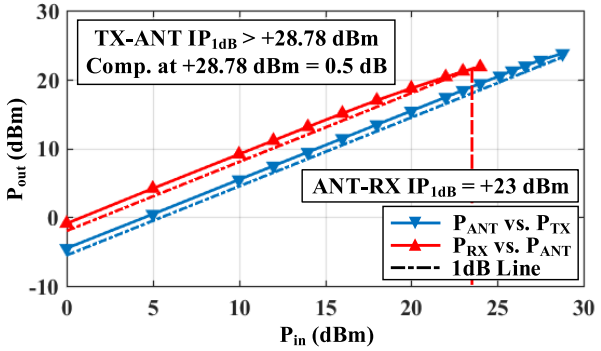

Fig. 28. Measured TX-ANT $IP_{1\,dB}$ and ANT-RX $IP_{1\,dB}$ at 2.35 GHz ($V_C = 28$ V).

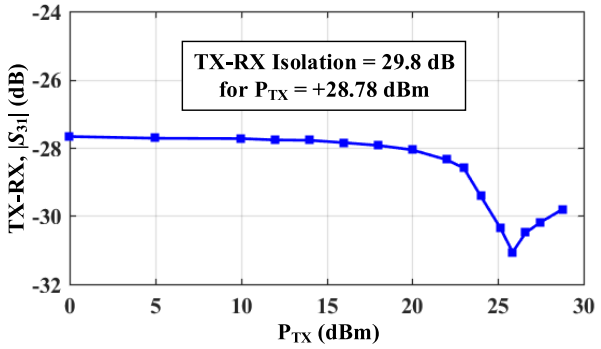

Fig. 29. Measured TX-RX isolation versus TX power at 2.35 GHz ($V_C = 28$ V).

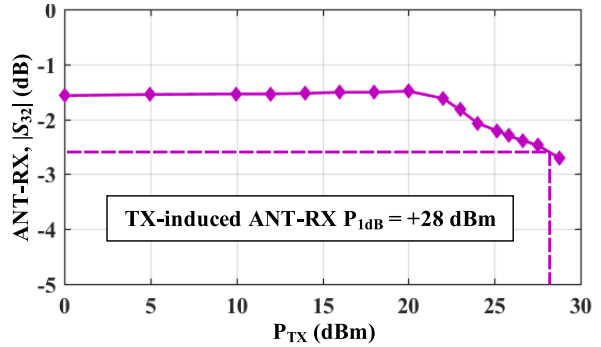

Fig. 30. Measured TX-induced ANT-RX $P_{1\,dB}$ at 2.35 GHz($V_C = 28$ V).

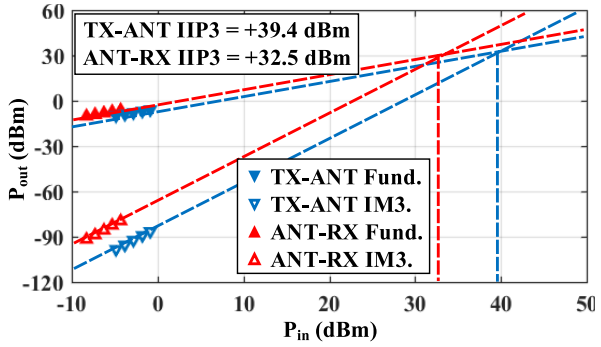

Fig. 31. Measured TX-ANT and ANT-RX IIP3s at the center frequency of 2.35 GHz ($V_C = 28$ V).

stage could be analyzed and the noise-canceling technique of the CS-stage can be utilized.

As shown in Fig. 28, the measured TX-ANT input $P_{1\,dB}$ is greater than 28.78 dBm (limited by the measurement setup), at which point the compression is only 0.5 dB, while the measured ANT-RX input $P_{1\,dB}$ is 23 dBm. Fig. 29 shows the TX-RX isolation is 29.8 dB for TX input power is 28.78 dBm. Meanwhile, as depicted in Fig. 30, the measured TX-induced ANT-RX $P_{1\,dB}$ is 28 dBm. Fig. 31 shows the measured TX-ANT and ANT-RX IIP3s are 39.4 and 32.5 dBm, respectively.

The performance summary of the proposed QC and comparison with the state of the arts are shown in Table I. Compared to the relevant researches, the proposed QC has a competitive performance of the −20-dB operating frequency range, low RX NF, and high power handling.

V. Conclusion

In this article, a reconfigurable wideband QC using a wideband 180° hybrid, a reconfigurable bidirectional in-phase stage, and a nonreciprocal out-of-phase stage is proposed. The slotline-based wideband 180° hybrid is introduced to achieve the wideband high TX-RX isolation. Besides, the bidirectional in-phase stage and the nonreciprocal out-of-phase stage are utilized to obtain a specific power-split ratio for the low insertion loss and high ANT-TX isolation. By using the unequal power split, such QC is without the fundamental 3-dB loss seen in reciprocal ANT interfaces. Meanwhile, a reconfigurable inter-stage matching network is implemented to further enhance the TX-RX isolation. Then, a reconfigurable wideband QC is implemented, fabricated, and measured. The measured in-band TX-RX isolation is greater than 27 dB over the 49.5% fractional bandwidth (i.e., 1.75–2.9 GHz). The RX insertion loss is 1.0–1.9 dB and the minimum in-band RX NF is 3.4 dB. Meanwhile, the measured TX input $P_{1\,dB}$ is greater than 28.78 dBm, while the RX input $P_{1\,dB}$ is 23 dBm. The TX-induced ANT-RX $P_{1\,dB}$ is measured to be 28 dBm.

Appendix

To investigate the power-split characteristic of the circuits in Fig. 5, an asymmetrical three-port network is introduced from [12]. As shown in Fig. 5(a), assuming the voltage at the T-junction is V_0 and the output powers are in a k_t:1 ratio. Then, the output powers at Port t2 and Port t3 could be expressed as

$$\begin{aligned} P_{2,t} &= \left|\frac{{V_{2,R}}^2}{R_{2,t}}\right| \\ &= \left|\frac{R_{2,t}}{{Z_{2,t}}^2}\right| {V_0}^2 \\ &= \frac{k_t}{k_t+1} P_{in} \end{aligned} \tag{19}$$

$$\begin{aligned} P_{3,t} &= \left|\frac{{V_{3,R}}^2}{R_{3,t}}\right| \\ &= \left|\frac{R_{3,t}}{{Z_{3,t}}^2}\right| {V_0}^2 \\ &= \frac{1}{k_t+1} P_{in} \end{aligned} \tag{20}$$

where P_{in} is the input power to the matched T-junction, $Z_i = R_i + jX_i$, and $V_{i,R}$ is the voltage at the resistive portion ($i = 2, 3$). Therefore, the load impedance of Port t2 and Port t3 should meet the following condition:

$$k_t = \left|\frac{\text{Real}(Z_{2,t})}{\text{Real}(Z_{3,t})} \times \frac{Z_{3,t}^2}{Z_{2,t}^2}\right|. \tag{21}$$

For a divider with $\lambda/4$ transmission lines, as shown in Fig. 5(b), the input impedance looking to Port d2 is

$$Z'_{2,d} = Z_C \frac{Z_{2,d} + jZ_C \tan\theta_C}{Z_C + jZ_{2,d} \tan\theta_C}. \tag{22}$$

Note that, for $\theta_C = 90°$, the $Z'_{2,d}$ is simplified as

$$Z'_{2,d} = \frac{Z_C^2}{Z_{2,d}}. \tag{23}$$

Meanwhile, the $Z'_{3,d}$ could be obtained similarly. Assume the output powers are in a k_d:1 ratio, thus the relation between the power-split ratio and load impedance could be as

$$k_d = \left| \frac{\mathrm{Real}\left(Z_C^2/Z_{2,d}\right)}{\mathrm{Real}\left(Z_C^2/Z_{3,d}\right)} \times \frac{\left(Z_C^2/Z_{3,d}\right)^2}{\left(Z_C^2/Z_{2,d}\right)^2} \right|. \tag{24}$$

REFERENCES

[1] G. Krishnamurthy and K. G. Gard, "Time division multiplexing front-ends for multiantenna integrated wireless receivers," *IEEE Trans. Circuits Syst. I, Reg. Papers*, vol. 57, no. 6, pp. 1231–1243, Jun. 2010.

[2] G. Castellano, D. Montanari, D. De Caro, D. Manstretta, and A. G. M. Strollo, "An efficient digital background control for hybrid transformer-based receivers," *IEEE Trans. Circuits Syst. I, Reg. Papers*, vol. 64, no. 12, pp. 3068–3080, Dec. 2017.

[3] M. Duarte, C. Dick, and A. Sabharwal, "Experiment-driven characterization of full-duplex wireless systems," *IEEE Trans. Wireless Commun.*, vol. 11, no. 12, pp. 4296–4307, Dec. 2012.

[4] D. Yang, H. Yuksel, and A. Molnar, "A wideband highly integrated and widely tunable transceiver for in-band full-duplex communication," *IEEE J. Solid-State Circuits*, vol. 50, no. 5, pp. 1189–1202, May 2015.

[5] D.-J. van den Broek, E. A. M. Klumperink, and B. Nauta, "An in-band full-duplex radio receiver with a passive vector modulator downmixer for self-interference cancellation," *IEEE J. Solid-State Circuits*, vol. 50, no. 12, pp. 3003–3014, Dec. 2015.

[6] J. Zhou *et al.*, "Integrated full duplex radios," *IEEE Commun. Mag.*, vol. 55, no. 4, pp. 142–151, Apr. 2017.

[7] T. Zhang, C. Su, A. Najafi, and J. C. Rudell, "Wideband dual-injection path self-interference cancellation architecture for full-duplex transceivers," *IEEE J. Solid-State Circuits*, vol. 53, no. 6, pp. 1563–1576, Jun. 2018.

[8] T. Dinc and H. Krishnaswamy, "A T/R antenna pair with polarization-based reconfigurable wideband self-interference cancellation for simultaneous transmit and receive," in *IEEE MTT-S Int. Microw. Symp. Dig.*, May 2015, pp. 1–4.

[9] M. Elkholy, M. Mikhemar, H. Darabi, and K. Entesari, "Low-loss integrated passive CMOS electrical balance duplexers with single-ended LNA," *IEEE Trans. Microw. Theory Techn.*, vol. 64, no. 5, pp. 1544–1559, May 2016.

[10] B. van Liempd *et al.*, "A +70-dBm IIP3 electrical-balance duplexer for highly integrated tunable front-ends," *IEEE Trans. Microw. Theory Techn.*, vol. 64, no. 12, pp. 4274–4286, Dec. 2016.

[11] G. Qi, B. van Liempd, P.-I. Mak, R. P. Martins, and J. Craninckx, "A SAW-less tunable RF front end for FDD and IBFD combining an electrical-balance duplexer and a switched-LC N-Path LNA," *IEEE J. Solid-State Circuits*, vol. 53, no. 5, pp. 1431–1442, May 2018.

[12] D. M. Pozar, *Microwave Engineering*, 4th ed. New York, NY, USA: Wiley, 2011.

[13] S. Tanaka, N. Shimomura, and K. Ohtake, "Active circulators—The realization of circulators using transistors," *Proc. IEEE*, vol. 53, no. 3, pp. 260–267, Mar. 1965.

[14] G. Carchon and B. Nanwelaers, "Power and noise limitations of active circulators," *IEEE Trans. Microw. Theory Techn.*, vol. 48, no. 2, pp. 316–319, Feb. 2000.

[15] K. Fang and J. F. Burkwalter, "A tunable 5–7 GHz distributed active quasi-circulator with 18-dBm output power in CMOS SOI," *IEEE Microw. Wireless Compon. Lett.*, vol. 27, no. 5, pp. 998–1000, Nov. 2017.

[16] S. Jain, A. Agrawal, M. Johnson, and A. Natarajan, "A 0.55-to-0.9 GHz 2.7 dB NF full-duplex hybrid-coupler circulator with 56 MHz 40 dB TX SI suppression," in *IEEE Int. Solid-State Circuits Conf. (ISSCC) Dig. Tech. Papers*, Feb. 2018, pp. 400–402.

[17] A. Kord, D. L. Sounas, Z. Xiao, and A. Alù, "Broadband cyclic-symmetric magnetless circulators and theoretical bounds on their bandwidth," *IEEE Trans. Microw. Theory Techn.*, vol. 66, no. 12, pp. 5472–5481, Dec. 2018.

[18] M. Biedka, P. Rodgers, N. Gutierrez, T. LaRocca, and Y. E. Wang, "100 MHz to 1 GHz on-chip circulator with integrated driver amplifiers," in *IEEE MTT-S Int. Microw. Symp. Dig.*, Jun. 2019, pp. 1488–1491.

[19] A. Nagulu, M. Tymchenko, A. Alù, and H. Krishnaswamy, "Ultra compact, ultra wideband, DC-1 GHz CMOS circulator based on quasi-electrostatic wave propagation in commutated switched capacitor networks," in *Proc. IEEE Radio Freq. Integr. Circuits Symp. (RFIC)*, Aug. 2020, pp. 55–58.

[20] A. Nagulu, T. Chen, G. Zussman, and H. Krishnaswamy, "Multi-watt, 1-GHz CMOS circulator based on switched-capacitor clock boosting," *IEEE J. Solid-State Circuits*, vol. 55, no. 12, pp. 3308–3321, Dec. 2020.

[21] S. K. Cheung, T. P. Halloran, W. H. Weedon, and C. P. Caldwell, "MMIC-based quadrature hybrid quasi-circulators for simultaneous transmit and receive," *IEEE Trans. Microw. Theory Techn.*, vol. 58, no. 3, pp. 489–497, Mar. 2010.

[22] J.-F. Chang, J.-C. Kao, Y.-H. Lin, and H. Wang, "Design and analysis of 24-GHz active isolator and quasi-circulator," *IEEE Trans. Microw. Theory Techn.*, vol. 63, no. 8, pp. 2638–2649, Aug. 2015.

[23] M. Porranzl, C. Wagner, H. Jaeger, and A. Stelzer, "High bandwidth of 8 GHz active quasi-circulator with integrated digital leakage canceler in SiGe BICMOS technology for automotive radar systems," in *IEEE MTT-S Int. Microw. Symp. Dig.*, May 2016, pp. 1–3.

[24] S. A. Ayati, D. Mandal, B. Bakkaloglu, and S. Kiaei, "Integrated quasi-circulator with RF leakage cancellation for full-duplex wireless transceivers," *IEEE Trans. Microw. Theory Techn.*, vol. 66, no. 3, pp. 1421–1430, Mar. 2018.

[25] Z. Deng, H. J. Qian, and X. Luo, "Tunable quasi-circulator based on a compact fully-reconfigurable 180° hybrid for full-duplex transceivers," *IEEE Trans. Circuits Syst. I, Reg. Papers*, vol. 66, no. 8, pp. 2949–2962, Aug. 2019.

[26] W. Chen, Y. Shu, Z. Deng, H. J. Qian, and X. Luo, "A wideband quasi-circulator with low NF and high P1dB using noise-canceling technique," in *IEEE MTT-S Int. Microw. Symp. Dig.*, Jun. 2019, pp. 587–590.

[27] M. Palomba, D. Palombini, S. Colangeli, W. Ciccognani, and E. Limiti, "Broadband nonreciprocal phase shifter design technique," *IEEE Trans. Microw. Theory Techn.*, vol. 66, no. 4, pp. 1964–1972, Apr. 2018.

[28] M. E. Bialkowski and Y. Wang, "Wideband microstrip 180° hybrid utilizing ground slots," *IEEE Microw. Wireless Compon. Lett.*, vol. 20, no. 9, pp. 495–497, Sep. 2010.

[29] H. Zhang, X. Fan, and E. S. Sinencio, "A low-power, linearized, ultra-wideband LNA design technique," *IEEE J. Solid-State Circuits*, vol. 44, no. 2, pp. 320–330, Feb. 2009.

[30] F. Bruccoleri, E. A. M. Klumperink, and B. Nauta, "Wide-band CMOS low-noise amplifier exploiting thermal noise canceling," *IEEE J. Solid-State Circuits*, vol. 39, no. 2, pp. 275–282, Feb. 2004.

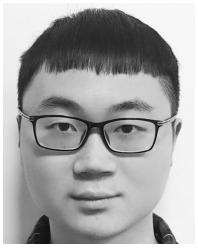

Wen Chen (Graduate Student Member, IEEE) received the B.E. degree in microelectronics from the University of Electronic Science and Technology of China, Chengdu, China, in 2019, where he is currently pursuing the Ph.D. degree in electronic science and technology.

His research interests include the wideband microwave/millimeter-wave circulator, oscillator, and frequency synthesizer.

Mr. Chen was a recipient of the China National Scholarship in 2016 and 2017.

Zhixian Deng (Graduate Student Member, IEEE) received the B.E. degree in microelectronics science and engineering from the University of Electronic Science and Technology of China, Chengdu, China, in 2019, where he is currently pursuing the Ph.D. degree in electronic science and technology.

His research interests include the reconfigurable microwave/millimeter-wave transceiver and passive components, especially integrated circuits.

Mr. Deng was a recipient of the IEEE IMS Student Design Competition Award from 2017 to 2019.

Yiyang Shu (Graduate Student Member, IEEE) received the B.E. degree in microelectronics from the University of Electronic Science and Technology of China (UESTC), Chengdu, China, in 2016, where he is currently pursuing the Ph.D. degree in microelectronics and solid state electronics.

His research interests include the integrated wideband microwave/millimeter-wave/terahertz oscillator and frequency synthesizer.

Mr. Shu was a recipient of the 2020–2021 IEEE SSCS Predoctoral Achievement Award, the 2020 IEEE MTT-Society Graduate Fellowship Award, the IEEE IWS Best Student Paper Award in 2018, the IEEE IMS Student Design Competition Award in 2018, and the IEEE RFIT Student Design Competition Award in 2016. He received the UESTC Distinguished Student Award (highest honor for students in UESTC) in 2020.

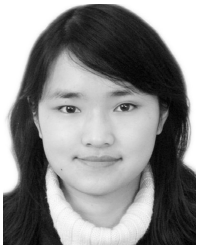

Huizhen Jenny Qian (Member, IEEE) received the B.E., master's, and Ph.D. degrees in electronic engineering from the University of Electronic Science and Technology of China (UESTC), Chengdu, China, in 2008, 2011, and 2018, respectively.

Since 2019, she has been a Faculty Member with the Center for Integrated Circuits, UESTC, where she is currently an Associate Professor. Her research interests include the wideband microwave/millimeter-wave transceiver, reconfigurable passive circuits, and ON-chip array systems.

Dr. Qian was a recipient/co-recipient of the 2018 IEEE MTT-Society Graduate Fellowship Award, the IEEE IWS Best Student Paper Awards in 2015 and 2018, the IEEE IMS Student Design Competition Awards in 2017 and 2018, and the IEEE RFIT Best Student Paper Awards in 2016 and 2019.

Xun Luo (Senior Member, IEEE) received the B.E. and Ph.D. degrees in electronic engineering from the University of Electronic Science and Technology of China (UESTC), Chengdu, China, in 2005 and 2011, respectively.

From 2010 to 2013, he was with Huawei Technologies Company, Ltd., Shenzhen, China, as the Project Manager to guide research and development projects of multi-band microwave/millimeterwave (mm-wave) integrated systems for backhaul and wireless communication. He was an Assistant Professor with the Department of Microelectronics, Delft University of Technology, Delft, The Netherlands. Since 2015, he has been with UESTC as a Full Professor, where he has been appointed as the Executive Director of the Center for Integrated Circuits. Since 2020, he has been the Head of the Center for Advanced Semiconductor and Integrated Micro-System, UESTC. He has authored or coauthored more than 100 journal and conference papers. He holds 33 patents. His research interests include the RF/microwave/mm-wave integrated circuits, multiple-resonance terahertz (THz) modules, multi-bands backhaul/wireless systems, reconfigurable passive circuits, smart antenna, and system in package.

Dr. Luo is a Technical Program Committee Member of the IEEE International Microwave Symposium (IMS), the IEEE Radio Frequency Integrated Circuits Symposium (RFIC), and the IEEE International Wireless Symposium (IWS). He is also the Technical Committee Member of the MTT-4 on Microwave Passive Components and Transmission Line Structures, the MTT-5 on Filters, and the MTT-23 on Wireless Communications. He is the Vice-Chair of the IEEE MTT-Society Chengdu Chapter. He was bestowed by China as the China Overseas Chinese Contribution Award in 2016. He received the UESTC 2016–2020 Outstanding Scientific Researcher Award, the UESTC Distinguished Innovation and Teaching Award in 2018, and the UESTC Outstanding Undergraduate Teaching Promotion Award in 2016. His research group BEAM X-Lab received multiple best paper awards and best design competition awards, including the IEEE IWS Best Student Paper Award in 2015 and 2018, the IEEE RFIT Best Student Paper Award in 2016 and 2019, the IEEE IMS Best Student Design Competition Award from 2017 to 2019 (four times), the IEEE IMS Sixty-Second Presentation Competition Award in 2019, and multiple best paper award finalists at the IEEE conferences. He is also the TPC Co-Chair of the IEEE IWS in 2018 and the IEEE RFIT in 2019. He serves as a Track Editor for the IEEE MICROWAVE AND WIRELESS COMPONENTS LETTERS and an Associate Editor for *IET Microwaves, Antennas & Propagation*.